Meccanica (2018) 53:2883–2896
https://doi.org/10.1007/s11012-018-0866-7

Numerical and experimental characterization of a double-orifice synthetic jet actuator

Matteo Chiatto · Francesco Capuano · Luigi de Luca

Received: 31 January 2018 / Accepted: 30 May 2018 / Published online: 15 June 2018

Abstract A complete investigation of a double-orifice synthetic jet actuator, focused on the device frequency response in terms of jet velocity, has been carried out. Numerical simulations have shown that, in many operation conditions, the flow within the actuator cavity can be considered as divided in two sub-volumes, each characterized by its own flow field. An analytical approach, based on the previous consideration, has allowed to obtain simple relationships for the three resonance frequencies and to provide further insights on the jets formation. The model has been validated through experimental tests carried out on two actuators manufactured in-house, having different geometrical and mechanical characteristics. Comparisons with the behavior of the twin single-orifice device have been discussed and useful considerations on the prediction of the actual formation of the synthetic jet are included .

Keywords Synthetic jet · Multiple orifices · Helmholtz resonance · Flow control

M. Chiatto (✉) · F. Capuano · L. de Luca
Department of Industrial Engineering, Universitá degli Studi di Napoli "Federico II", P.le Tecchio 80, 80125 Naples, Italy
e-mail: matteo.chiatto@unina.it

1 Introduction

Synthetic jet (SJ) actuators are a well-established technology widely used in different sectors. They have been applied in many problems, such as flow control [1], water spray vectoring [2], mixing enhancement [3], heat transfer [4], and many others.

A synthetic jet is an electromechanical device composed of a small cavity, which is sealed from one side by an elastic vibrating diaphragm, and from the other one it communicates with the external environment through one or more orifices (Fig. 1). A waveform electrical signal is used to excite the diaphragm, usually composed of a thin metallic shim combined with a piezo-ceramic element, producing a subsequent alternation of fluid (air) ejection and suction phases across the orifices. This motion results in a train of vortex rings that interact with each other and break up due to viscous dissipation, generating in the far field a downstream-directed turbulent jet. A major interest in these devices is related to the production of a non-zero average momentum rate, with a null average mass flow rate during an operation cycle. Moreover, its generation does not require any continuous fluid supply, because the jet is synthesized directly from the surrounding ambient fluid, as well established by Smith and Glezer [5] and Cater and Soria [6], among others.

The scientific literature quotes several works focused on the design and the application of these

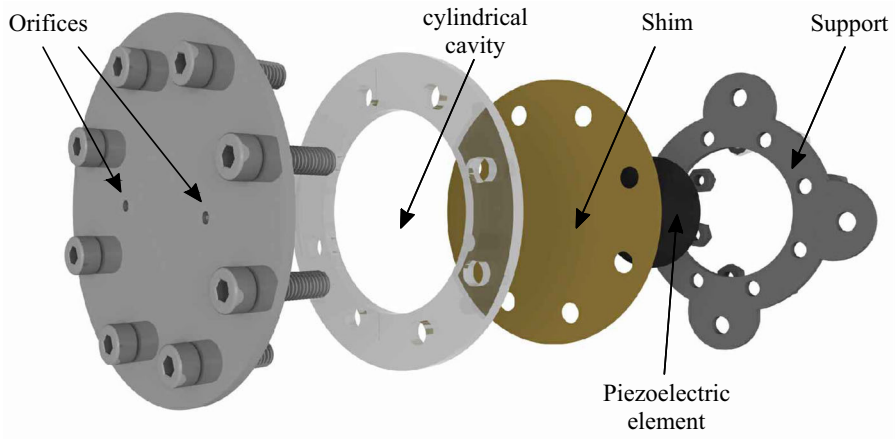

Fig. 1 Sketch of a two-orifice synthetic jet actuator

devices, usually restricted to a single-orifice configuration, favoring systems with several single-orifice devices over few multiple-orifice actuators. On the one hand, this preference is related to high velocity output requirements, while on the other hand it lies into a difficult prediction of a multiple-orifice device behavior. These devices can be very useful when many close orifices are required in a small space, both in flow control and heat transfer applications. It clearly appears the need to deeply investigate the multiple-orifice configurations to understand their fluid-dynamic behavior and to develop different tools for design and manufacturing purposes.

A first study of a two-orifice actuator was conducted by Watson et al. [7], who experimentally studied the fluid-structure interaction produced by this device, varying the spacing between the orifices. They argued that the resulting total circulation in a two-orifice configuration is greater than that produced by a single-orifice device with the same exit area. From a numerical point of view, instead, an investigation was carried out by means of unsteady incompressible laminar simulations by Riazi and Ahmed [8], who suggested the existence of a minimum spacing to avoid any vortex interaction related to the main device quantities. Very recently Sakakibara et al. [9] carried out an experimental characterization of a high-speed piston-driven SJ actuator for different configurations (single and multiple holes) and diameters, with cylinder pressure measurements and flow visualization.

However, a multiple-orifice actuator has revealed its maximum potential in electronic component cooling problems. In this context, Chaudhari at al. [10] first and Mangate et al. [11] later explored the thermal performances of an impinging SJ device (with additional satellite orifices around the main one). Experimental measurements revealed that a multiple-orifice device exhibits a better heat dissipation ($\simeq 12\%$) with respect to a single centered orifice and that it can be successfully considered a valid and cost-effective cooling device as compared to a classical fan. Two-orifice configurations could be favourably employed in flow control applications when an array distribution of orifices is requested along the spanwise direction of flow, as an alternative of slotted configurations. Clearly, efficiency considerations should drive the choice among the available configurations, and a proper efficiency modeling should be developed for the double- or multiple-orifice configurations, following the guidelines given in the basic paper by Girfoglio et al. [12] referring to the standard single-orifice device.

The frequency response of a SJ actuator can be successfully predicted through the definition of a low-order model, i.e. the so called lumped element model (LEM), which represents a very practical tool to obtain the time variation of the thermodynamic quantities inside the cavity, as well as the jet velocity at the orifice, as functions of the operating frequency (Chiatto et al. [13] and references cited herein).

This work aims at presenting a complete characterization of a double-orifice SJ actuator, shedding light on its frequency response in terms of air jet velocity. An analytical approach, based on the fluid dynamic behavior argued by means of numerical simulations, will allow to obtain simple relationships for the resonance frequencies and further insights on

its formation. The model will be validated through systematic experimental tests carried out on two home-made actuators, having different geometrical and mechanical characteristics.

2 Flow dimensionless quantities

It is well known that the behavior of a synthetic jet actuator can be described through a finite number of dimensionless quantities, see e.g. [14, 15].

One of the main parameter characterizing the jet strength is the so called stroke length $\bar{L}$, which represents the average distance covered downstream by the fluid during the ejection phase only:

$$\bar{L} = \int_0^{T/2} U(t)dt \tag{1}$$

where T is the actuation period and $U(t)$ represents the phase-averaged jet velocity at the orifice exit, and t is the time. Starting from this quantity, it is convenient to introduce a proper reference velocity through the relation $\bar{U} = \bar{L}/T$, commonly referred to as stroke length velocity.

Velocity measurements are frequently acquired in the saddle point, i.e. the stagnation point which separates the near field region, where the flow is directed towards the cavity during the suction phase, from the far field, where the jet is always directed downstream and is well established. According to classic literature findings [5, 16], the saddle point velocity, U_e, is roughly 1.1 times the stroke length velocity, which in turn, for sine time variation of the exit velocity, is related to its peak value by $\bar{U} = U_{max}/\pi$. Thus, to compare experimental measurements of the external velocity in the saddle point to numerical computations of the velocity peak value U_{max} at the orifice, the following relationship can be used:

$$U_e = 1.1\frac{U_{max}}{\pi} \tag{2}$$

A significant Reynolds number, based on the diameter of the orifice d and on the averaged jet velocity, is given by:

$$Re = \frac{\bar{U}d}{\nu} \tag{3}$$

with ν being the kinematic viscosity coefficient of air.

The Stokes number can be defined as:

$$S = \sqrt{\frac{\omega d^2}{\nu}} \tag{4}$$

with ω being related to the actuation cyclic frequency f by $\omega = 2\pi f$. As a measure of the ratio between the unsteady and the viscous forces, a high Stokes number results in a thinner boundary layer along the orifice wall and therefore in a top-hat shaped inner velocity profile; on the other hand, a low Stokes number results in a change from a top-hat to a near-parabolic shaped velocity profile [17].

Finally, the Strouhal number can be introduced as:

$$St = \frac{\omega d}{\bar{U}} \tag{5}$$

Since the Strouhal number represents the ratio of the unsteady forces to the inertial ones, it plays a crucial role in the jet formation process. Very often the dimensionless stroke length, $L = \bar{L}/d$, is also used, which is related to the Strouhal number by the relation $St = 2\pi/L$.

The Reynolds, Stokes and Strouhal numbers are clearly not independent of each other, since it holds:

$$St = \frac{S^2}{Re} \tag{6}$$

Hence, only two dimensionless numbers are sufficient to completely characterize the state of a SJ device; they have been introduced here for their specific influence on the jet formation and the characterization of the operative conditions, that will be analyzed in the subsequent sections.

3 Numerical simulations

It has to be preliminarily stressed that the numerical simulations reported hereafter have been carried out only for the aim of obtaining overall qualitative insights on the development of the flow field inside the cavity. Detailed data concerned with the external environment as well as local behaviors of mean and turbulent quantities are beyond the scope of the present paper and will be subject of future work.

Unsteady incompressible simulations, performed with OpenFOAM, have been carried out to simulate

the flow behavior within the cavity as well as in the external field surrounding the orifice exit. OpenFOAM is an open-source CFD toolbox which is widely used nowadays for a large variety of thermo-fluid-dynamics problems. The grid developed for the computation is fully 3D and is composed of regular hexahedral elements, modeling the whole geometry of the actuator.

The orifices have a diameter of $d = 2$ mm with a height (or length) of $h = 2$ mm. Two different cavity heights ($H/d = 1, 10$), with the same cavity diameter ($D/d = 20$), have been considered to understand how the flow behaves within the cavity. An actuation frequency of $f = 1000$ Hz, corresponding to a typical operating value, has been set for all the simulations.

The reference system has been defined as follows: the origin is coincident with the center of the cavity bottom plane (i.e., the diaphragm), the X axis is directed along the streamwise direction, the Y axis crosses the orifices centers and is orthogonal to their axes, while the Z axis lies in the cavity plane. A detailed view of the mesh around an orifice, in the cavity bottom plane (X = 0), is presented in Fig. 2; note that the same geometry has been retained from the cavity to the end of the computational domain. The grid points number has been assessed at the end of a series of preliminary numerical tests (not reported herein) to verify the convergence of the flow field qualitative features. Figure 3 reports a sketch of a X–Y cross section of the computational domain. Due to the symmetry of the flow with respect to the X axis, only half of the device is represented. Regarding boundary conditions, on the fixed solid walls, indicated with a thick line, a "no-slip" condition has been employed, while the boundaries of the surrounding environment

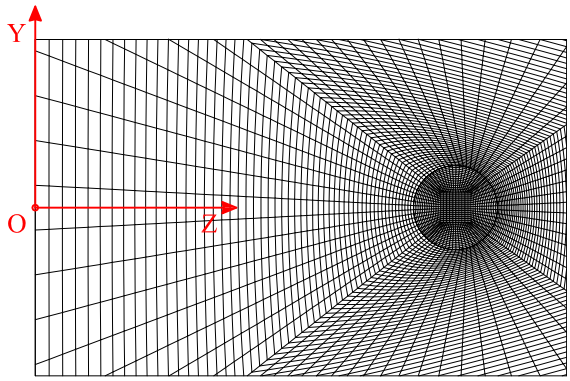

Fig. 2 Mesh detail around an orifice, X=0

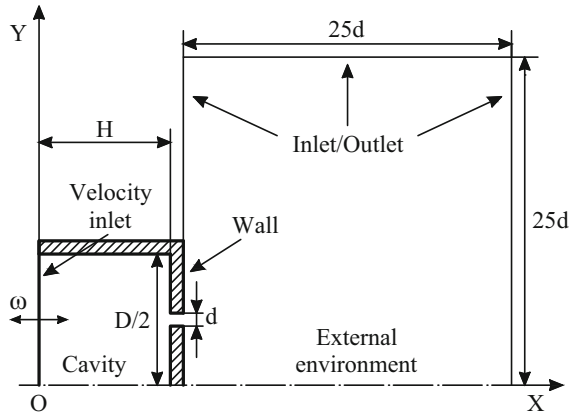

Fig. 3 Computational domain with the boundary conditions

are equipped with an "inlet/outlet" condition, and a velocity inlet condition has been imposed at the moving diaphragm to model the effect of the oscillating diaphragm (among others, see the recent contribution by Zhou et al. [17]),

$$u(t) = \Delta x_w \omega \cos(\omega t) \tag{7}$$

where Δx_w is the diaphragm average linear displacement. For these simulations a typical displacement of $\Delta x_w \simeq 25\,\mu$m has been considered (Krishnan and Mohseni [18]).

To ensure an adequate spatial resolution of the flow structures, the grid has been refined in the actuator orifices, in the region around the jet exit and within the cavity. The cavity cell size has been preserved for the different simulations, meaning that the cells number within the cavity for the case $H/d = 10$ is 10 times the one for $H/d = 1$; the computational domain of the external environment extends by $25\,d$ in both the radial and streamwise directions. The pimpleFoam solver was employed, with a pressure accuracy of 10^{-7}. Time integration is carried out by means of a second-order accurate backward scheme. The time-step size was set to keep at least 10^2 time intervals for each cycle and to guarantee a Courant number lower than 0.5. The spatial discretization is based on centered second-order schemes. All the geometric and numerical quantities are summarized in Table 1.

Overall, these simulations aim at studying the basic behavior of the flow within the cavity so as to extract useful information to be transferred to a low-order model. In the post-processing phase, the application of the Q-criterion [19] to the phase-averaged velocity

Table 1 Numerical parameters of the CFD simulations

Cavity diameter, D/d	20
Cavity height, H/d	1, 10
Orifices height, h/d	1
Orifices distance, e/d	10
Cells number	1095500, 3561500
Reynolds number	$\simeq 2.5 \times 10^3$, $\simeq 10^3$
Stokes number	40
Strouhal number	0.64, 1.54

fields has allowed the identification of the vortical structures and their evolution in the whole domain.

With reference to the $H/d = 1$ case, the phase averaged iso-surfaces of Q, with the Q values being normalized with respect to the maximum value, coloured by the streamwise velocity component, are reported in Fig. 4. Four phases, corresponding to $t/T = 0.1, 0.3, 0.6$ and 0.9, have been considered; the continuous straight lines of each individual picture define the cavity cross section made by the X–Y plane passing through the orifice axes, with the orifice edges being hidden by the colored vortical structures. Note that the suction phase starts at mid-cycle, namely $t/T = 0.5$. These pictures clearly show the formation and the evolution of the vortex rings during the whole cycle. At $t/T = 0.1$ the ejection phase has already started, a couple of vortex rings are forming near the exit sections of the two orifices, while coherent structures related to the previous cycle can be still observed within the cavity. The vortices move downstream in the X direction as the cycle progresses, and a secondary instability occurs along their azimuthal direction leading to the break-up of the structures. Similarly, during the suction phase (t / T=0.6), another couple of vortices appear on the upper side of the cavity moving towards the diaphragm, whereas the external vortices completely lose their coherent shape.

Riazi and Ahmed [8] found that for an orifice centers distance, e, approximately greater than $1.5\,\bar{L}$, the vortex rings do not interact with each other. In the present case it is $e \simeq \bar{L}$, thus one could expect an interaction between the vortices a few diameters away from the exit plane, but, due to the very small cavity height, the vortices collide with the diaphragm and their natural development is not allowed.

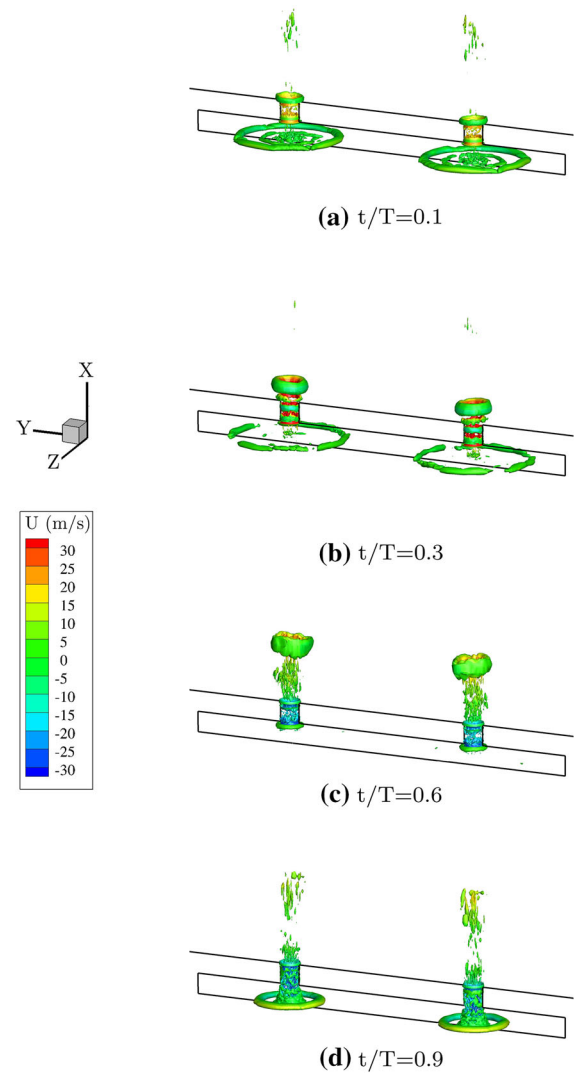

Fig. 4 Iso-surfaces of phase-averaged Q-criterion with the streamwise velocity for $H/d = 1$ case. Iso-surface plotted at $Q = 2.5 \times 10^{-3}$

A similar evolution has been found also for the $H/d = 10$ case, as shown in Fig. 5. This geometric configuration allows to follow not only the evolution of the forming vortices, but also the subsequent interaction with the previous ones. Indeed, the couple of vortices, developed during the suction phase of the previous cycle, move towards the diaphragm, losing their coherent structure. Note that applying the same boundary condition of Eq. (7), for a higher cavity height, results in a lower stroke length velocity. This case satisfies the Riazi and Ahmed condition, being $e > 2\,\bar{L}$, meaning that the vortex rings move both in

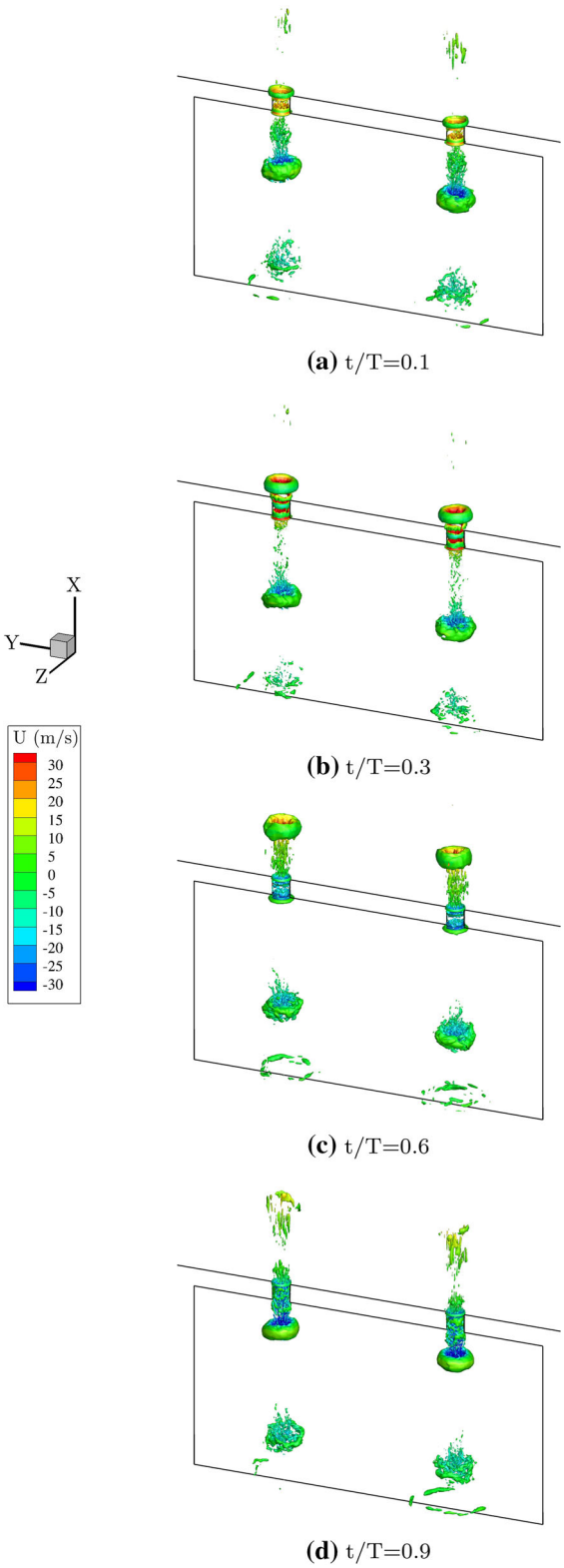

◀**Fig. 5** Iso-surfaces of phase-averaged Q-criterion coloured by the streamwise velocity for $H/d = 10$ case. Iso-surface plotted at $Q = 2.5 \times 10^{-3}$

the stream directions without interacting with each other. Figure 6 reports the phase-averaged streamlines in the X–Y plane superimposed on the vorticity field at $t/T = 0.5$, i.e. at the beginning of the suction phase; the division between the two sub-volumes determined by the central streamline directed upwards is clearly visible and further corroborates the previous analysis. The two green vortex structures present nearly in the middle of the two sub-cavities represent the couple of vortices, developed during the suction phase of the previous cycle, moving towards the diaphragm.

The design of a new actuator focuses on maximizing the device velocity response at a certain (resonance) frequency, with the possibility of reducing it by simply changing the power supply voltage. From a practical point of view, this results in a wide cavity with a tiny height, where the orifices are located in the opposite side of the diaphragm. This leads in practice to geometrical configurations with $H/d = 1$; thus, if one excludes the case with $e \simeq d$, very often the vortex rings do not have the possibility to interact with each other and the flow within the cavity can be considered as divided in two sub-cavities. For a very large cavity height the Riazi and Ahmed condition is often satisfied, leading to the same conclusion. Therefore,

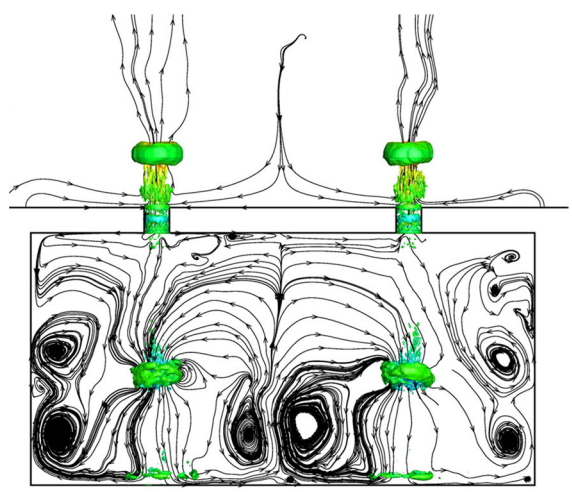

Fig. 6 Iso-surfaces of phase-averaged Q-criterion coloured by the streamwise velocity and streamlines for $H/d = 10$ and $t/T = 0.5$ case. Iso-surface plotted at $Q = 2.5 \times 10^{-3}$

as a first finding of this analysis, an effective lumped model of the double-orifice configuration should consider the device cavity as divided in two sub-volumes, with each of them being characterized by its own velocity and pressure.

4 LEM/analytical approach

In this section, a lumped model aimed to simulate the behavior of a double-orifice synthetic jet actuator will be developed, by taking advantage of the conclusions of the previous section. Following the basic approach of Chiatto et al. [13], the major elements of the actuator are: the oscillating diaphragm, the two (separated) cavities, and the two orifices. Note explicitly that two control volumes, with their own internal pressures, have to be considered.

Introducing two differential internal pressures, $p_{i,1}$ and $p_{i,2}$, one for each half-cavity, the diaphragm dynamics equation can be written as:

$$\ddot{x}_w + 2\zeta_w \omega_w \dot{x}_w + \omega_w^2 x_w = \omega_w^2 \Delta x_w \sin \omega t - \frac{(p_{i,1} + p_{i,2}) A_w/2}{m_{wt}} \tag{8}$$

where $x_w(t)$ is the diaphragm (average) displacement at a generic time instant t, ζ_w is the actual damping ratio of the diaphragm, ω_w its natural frequency, Δx_w is the average linear diaphragm displacement due to the application of a certain voltage to the piezo-element, ω is the operating frequency, and the dot superscript stands for time derivative. Moreover, A_w is the diaphragm surface area and m_{wt} is the diaphragm total mass, including shim, piezo-element and air added mass.

The structural frequency of the composite diaphragm is defined as:

$$\omega_w = \sqrt{\frac{k_w}{m_{wt}}} \tag{9}$$

representing the uncoupled (first mode) natural frequency of the structural oscillator, where k_w is the diaphragm equivalent spring stiffness. Further details can be found in [13]. Note that a symmetric configuration leads to the same values for the differential internal pressures, with the possibility to simplify the entire system; here, for a matter of generality, they have been retained as two distinct quantities.

As mentioned before, two separate continuity equations must be written for each half-cavity:

$$\frac{(V_c/2)}{\gamma p_a} \frac{dp_{i,1}}{dt} - (A_w/2)\dot{x}_w = -A_{o,1} U_1 \tag{10}$$

$$\frac{(V_c/2)}{\gamma p_a} \frac{dp_{i,2}}{dt} - (A_w/2)\dot{x}_w = -A_{o,2} U_2 \tag{11}$$

where $V_c = A_w H$ is the cavity volume, $A_{o,1}$ and $A_{o,2}$ are the orifices areas, γ is the specific heat ratio of air, p_a is the external ambient pressure and U_1 and U_2 are the instantaneous flow velocities through the orifices.

Finally, the model is completed by the unsteady Bernoulli's equations, written for both the orifices:

$$\ddot{U_1} + \frac{K}{l_{e,1}} |U_1| \dot{U_1} + \omega_{H,1}^2 U_1 = \frac{A_w}{A_{o,1}} \omega_{H,1}^2 \dot{x}_w \tag{12}$$

$$\ddot{U_2} + \frac{K}{l_{e,2}} |U_2| \dot{U_2} + \omega_{H,2}^2 U_2 = \frac{A_w}{A_{o,2}} \omega_{H,2}^2 \dot{x}_w \tag{13}$$

being K the head loss coefficient, including the inviscid contribution (equal to unity) due to the kinetic energy recovery at ambient pressure, and minor (entrance/exit) losses. The distances between the two application points of the Bernoulli's equations are referred to as the modified (effective) lengths of the orifices, ($l_{e,1}$ and $l_{e,1}$). More details and typical values for K can be found in [20, 21]. The Helmholtz frequencies are defined as:

$$\omega_{H,1} = \sqrt{\frac{\gamma A_{o,1}^2 p_a/(V_c/2)}{\rho_a l_{e,1} A_{o,1}}} = \sqrt{\frac{k_{a,1}}{m_{a,1}}} \tag{14}$$

$$\omega_{H,2} = \sqrt{\frac{\gamma A_{o,2}^2 p_a/(V_c/2)}{\rho_a l_{e,2} A_{o,2}}} = \sqrt{\frac{k_{a,2}}{m_{a,2}}} \tag{15}$$

with $k_{a,1}$, $k_{a,2}$ and $m_{a,1}$ and $m_{a,2}$ being the equivalent stiffness of the air inside the cavities and the effective masses of the air at the orifices.

The actuator behavior can be modeled by resorting to the dynamics of a system of coupled oscillators. The first one, which describes the diaphragm motion, is characterized by the uncoupled natural frequency ω_w; while the other two, the acoustic oscillators, that model the dynamics of the masses of air at the orifices ($m_{a,1}$ and $m_{a,2}$), through their velocities U_1 and U_2, are characterized by their natural frequencies $\omega_{H,1}$ and

$\omega_{H,2}$. An external forcing due to the supply power also acts on the diaphragm dynamics.

It is worth noting that, in these conditions, the Helm-holtz oscillators are decoupled in terms of exit velocities, but they are forced by the same diaphragm average displacement. This statement can be clarified by looking at the schematic representation of the damped forced spring-mass oscillators system, reported in Fig. 7, where $k_w^{'} = \frac{\gamma p_a}{V_c} A_w^2$, $k_{wH,1} = k_{Hw,1} = \frac{\gamma p_a}{V_c} A_{o,1} A_w$ and $k_{wH,2} = k_{Hw,2} = \frac{\gamma p_a}{V_c} A_{o,2} A_w$. The damped spring-mass oscillator related to the diaphragm motion is practically the same as the one-orifice model [13], whatever the number of orifices is; for the acoustic oscillators, the damped spring-mass system within the cavity remains unchanged, but the stiffness of the air acting on the air mass within each orifice is halved.

By making the assumption of absence of damping effects, considering a symmetric configuration and imposing the temporal behavior of the free oscillations $\sim e^{j\omega_n t}$ to obtain the periodic stationary motion

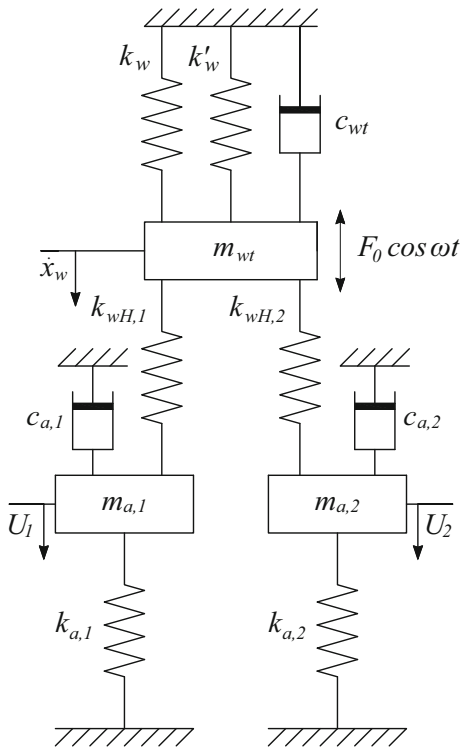

Fig. 7 Forced damped spring-mass schematic of a double-orifice SJ

solution, a closed-form analytical evaluation of the three natural coupled (or modified) frequencies, ω_n, can be obtained:

$$\omega_n^2 = \omega_{1,2}^2 = \frac{\Omega \pm \sqrt{\Omega^2 - 4(\omega_w^2 - \omega_{wc}^2)\omega_H^2}}{2} \tag{16}$$

$$\omega_n^2 = \omega_3^2 = \omega_H^2 \tag{17}$$

being $\Omega = \omega_w^2 + \omega_{wc}^2 + \omega_H^2$. The frequency ω_{wc} represents the natural frequency of the coupling spring made of the air enclosed within the cavity volume, V_c, acting on the oscillating diaphragm of mass m_w:

$$\omega_{wc} = \sqrt{\frac{\gamma A_w^2 p_a / V_c}{m_{wt}}} = \sqrt{\frac{\gamma A_w p_a}{m_{wt} H}} \tag{18}$$

For a double-orifice actuator, the first two eigenvalues are almost the same as the single-orifice configuration; the only difference lies in the presence of the $4\omega_{wc}^2\omega_H^2$ term, which represents the coupling between the oscillators. This term is always positive, meaning that the addition of an orifice increases the distance between the first two resonance frequencies. Moreover, a third eigenvalue equal to the Helmholtz natural frequency appears. Note that in the present case the Helmhotz's frequency has to be computed by referring to the half cavity; the ratio of this frequency to the one relative to the whole cavity is equal to $\sqrt{2}$, according to an historical result of Ingard [22].

As a summary, in the double-orifice configuration the actuator can exhibit at most three coupled resonance frequencies, that may not be straightforwardly observed during its working regime. This aspect will be further clarified in Sect. 5.

5 Experimental measurements

To experimentally validate the previous numerical and analytical results, two actuators (with different shim materials) have been manufactured and tested in order to study how the actuator response can be influenced by the oscillators coupling effects. The results have been compared also to those obtained by testing the corresponding one-orifice devices. The measurements have been carried out basically to characterize the frequency response of the devices in terms of air jet velocity.

The experimental rig is reported in Fig. 8. The actuators have been electrically excited with a sine signal generated through a USB Instruments DS1M12 or "Stingray" (which can work simultaneously as both signal generator and data-acquisition system) and then transmitted to a linear gain amplifier (EPA-104, Piezo Systems). Exit jet velocities were measured with two home-made Pitot tubes, with a 0.6 mm external diameter and a 0.4 mm internal diameter, connected with different pressure transducers (All Sensors and Honeywell pressure transducers with a range respectively of ± 0.25 and ± 2 in H_2O and an accuracy of 0.05 and 0.25 %) to ensure very low uncertainty values globally. The transducer pressure signals have been acquired with the same data-acquisition system (DS1M12). The probes were placed 1 diameter downstream of the nozzle exit section, conventionally representing the saddle point for different actuation frequencies; therefore, the velocity experimental measurements U_e and LEM predictions of peak jet velocity U_{max} are correlated to each other by means of Eq. (2). The experimental measurement uncertainty, estimated with standard procedures (see [23]), is lower than 6%.

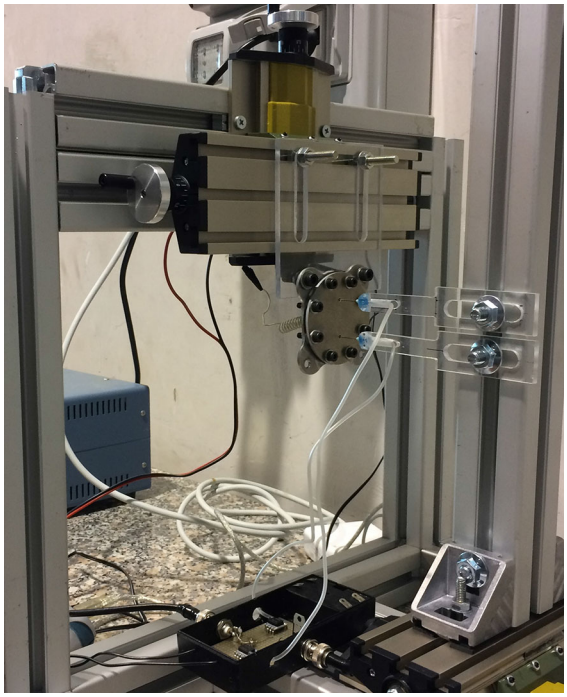

Fig. 8 Experimental rig

The basic characteristics of such actuators, one having the diaphragm in brass and the other one in aluminum, are reported in Table 2, while the geometrical and mechanical properties of the shim and of the piezo-electric element are reported in Table 3. All the devices have been entirely realized in house, using a two-component silver-filled epoxy resin (EPO-TEK E4110-LV resin) to bond the piezo-electric element (manufactured by PIEZO Inc.) to the metallic shims.

To gain more insight into the peculiarities of the double-orifice configuration, brass and aluminum twin devices have been manufactured, having the very same electro-mechanical properties, but equipped with a single orifice only. The relevant comparisons between the behavior of the two configurations will be discussed later on.

Considering first the brass diaphragm, the device frequency response, in terms of saddle point jet velocity for different cavity heights, is reported in Fig. 9. The findings are quite similar to a single-orifice configuration [13], but it is interesting to observe that, contrary to the prediction of the analytical model, the actuator exhibits only two resonance peaks, corresponding to the Helmholtz natural frequency, Eq. (17), where, as already observed, the volume of the half cavity has to be considered and therefore the actual frequency is scaled by a factor $\sqrt{2}$ with respect to the nominal value, and to the modified structural frequency given by the higher value solution arising from Eq. (16).

Furthermore, a peculiar behavior can be observed at low operating frequencies. As the actuation frequency decreases, all the curves should tend towards the so-called incompressible solution, which is the static solution (i.e., for zero frequency) of the equivalent forced damped spring-mass system, see [13]. This particular solution, reported in Eq. (19),

$$U_{inc} = (A_w/A_0)\omega\Delta x_w \tag{19}$$

Table 2 Geometrical characteristics of the tested actuators

Cavity diameter, D/d	21
Cavity height, H/d	0.75, 1.50, 2.25, 3.00, 3.75
Orifices height, h/d	1
Orifices distance, e/d	12.5

Table 3 Geometrical and mechanical properties of the shim and of the piezo-electric elements

	Brass	Aluminum
Shim		
Diameter, D_s (mm)	42	42
Thickness, th_s (mm)	0.4	0.25
Young's module (Pa)	9.7×10^{10}	7.31×10^{10}
Poisson's module	0.36	0.31
Density (kg/m^3)	8490	2780
Piezo-electric		
Diameter, D_p (mm)	31.8	31.8
Thickness, th_p (mm)	0.191	0.191
Young's module (Pa)	6.6×10^{10}	6.6×10^{10}
Poisson's module	0.31	0.31
Density (kg/m^3)	7800	7800

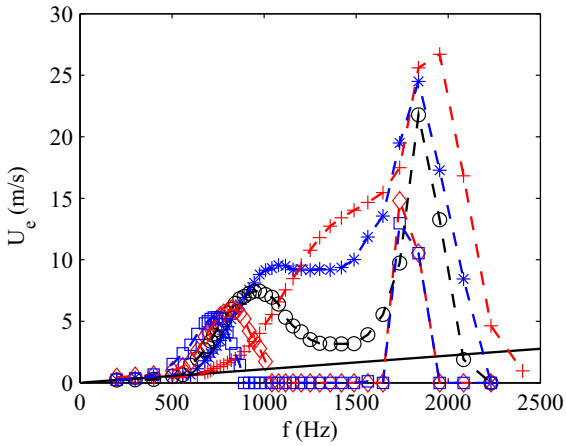

Fig. 9 Frequency response of the brass SJ double-orifice actuator. The "plus" marker represents the $H/d = 0.75$ case, "asterisk" stands for $H/d = 1.50$, "circle" for $H/d = 2.25$, "diamond" for $H/d = 3.00$ and "square" for $H/d = 3.75$. The black line represents the incompressible solution, Eq. (19)

physically expresses the fact that the volume rate of air expelled trough the orifice is equal to the volume rate entering the cavity as consequence of the membrane displacement. The incompressible solution is depicted in Fig. 9 by a black continuous straight line. This behavior can be clearly observed in Fig. 9, where all curves, for low frequencies, lie on the incompressible one. It is also interesting to study how the device response leaves the incompressible solution at different cavity heights. Indeed, because the Helmholtz resonance frequency is inversely proportional to the cavity volume, its amplifications occur first (lower frequencies) for greater cavity heights, resulting in an early deviation.

A very similar behavior can be observed for the aluminum diaphragm, as reported in Fig. 10. Remembering that the Helmholtz natural frequency scales as $\sim H^{-1/2}$, one observes that it decreases as the cavity height increases. The structural frequency, instead, for uncoupled oscillators is independent of the cavity height; in the cases here analyzed, due to limited coupling effects, a slight tendency towards higher values can be observed for both diaphragm configurations. Note that the frequency resolution of the present measurement has been limited by the acquisition system.

In order to examine in more detail the experimental findings, for the case of the aluminum device, the resonance frequencies, extracted from the experimental data, have been reported in Table 4 (second line), together with the corresponding ones of the single-orifice configuration (first line). In this case, $f_{H,e}$ represents the experimental Helmholtz resonance frequency and $f_{w,e}$ the structural one; for clarity, also the Helmholtz natural frequency (f_H) has been reported.

It is worth comparing the resonance frequencies for the two configurations (single- and double-orifice). Bearing in mind Table 4, the prediction that an

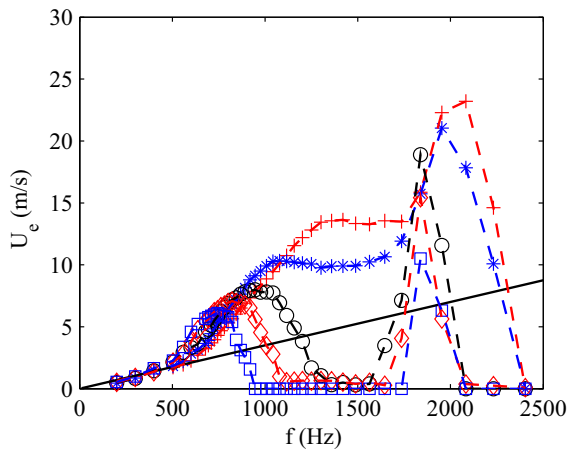

Fig. 10 Frequency response of the aluminum SJ double-orifice actuator. The "plus" marker represents the $H/d = 0.75$ case, "asterisk" stands for $H/d = 1.50$, "circle" for $H/d = 2.25$, "diamond" for $H/d = 3.00$ and "square" for $H/d = 3.75$. The black line represents the incompressible solution, Eq. (19)

Table 4 Aluminum actuator experimental resonance frequencies, f (Hz)

Case	$f_{H,e}$	$f_{w,e}$	f_H
H/d = 0.75	976	1953	1007
	1420	2083	1424
H/d = 1.50	744	1953	736
	1078	1953	1041
H/d = 2.25	679	1838	623
	946	1838	881
H/d = 3.00	558	1838	561
	822	1838	822
H/d = 3.75	504	1838	523
	744	1838	744

The 1st line refers to the single-orifice device, the 2nd to the double-orifice configuration

additional orifice should increase the Helmholtz frequency by a factor of $\simeq \sqrt{2}$ is actually verified. The structural frequency remains almost unchanged for the different configurations; the only mismatch lies in the $H\ /\ d = 0.75$ case. Actually, looking at Fig. 10, it is clear that the structural resonance peak should be located between 1953 and 2083 Hz, which is however compatible with the expected result.

Again, as the actuation frequency decreases, all the curves tend towards the incompressible solution, as already discussed before. Note that, in the very low frequency regime the velocity magnitude is comparable to the transducer uncertainty, making the experimental measurements meaningless.

6 Further insights on the formation process

It is generally more convenient to face the jet formation problem with the aid of the Stokes–Strouhal numbers plane. Using the definition of Eq. (5), the Holman criterion [24] can be written as $St^{-1} > C$, where C is a certain constant which depends on the geometrical characteristic of the orifice. For round axisymmetric orifices it is $C \simeq 0.08$. It gives the minimum air ejection velocity issuing from the orifice for the formation of the jet at a given operation frequency, and therefore in dimensionless terms (Stokes–Strouhal numbers plane) the formation boundary is represented by a straight line parallel to the abscissas axis. All the conditions above this line satisfy the formation criterion. Figures 11 and 12 can be used to compare the frequency response for the single and the double-orifices for the selected cases of $H/d = 0.75$ and 2.25. For the sake of completeness, the corresponding incompressible solutions have also been reported. It should be outlined that, bearing in mind Eq. (19), also such solutions can be easily represented as constant Strouhal number values, and that, since the cavity volume of the double-orifice configuration is the half of the single-orifice case, namely the surface area A_w is the half, the Strouhal number of the incompressible solution for the double-orifice configuration is the half of the single-orifice case.

For both configurations, the formation limit (continuous line $St^{-1} = 0.08$) is well below the incompressible solutions (red dashed line), allowing the synthetic jet formation. For frequencies in between the resonance ones and for the high cavity height, the amplifications with respect to the incompressible solutions are poor due to high nonlinear fluidic damping effects, the formation criterion is not satisfied, and the device response is null. This phenomenon has been already observed in literature for a single-orifice device, e.g., by Gallas et al. [25] (who attributed to it the absence of the first resonance peak for one of their devices) [13, 26, 27]. These remarks

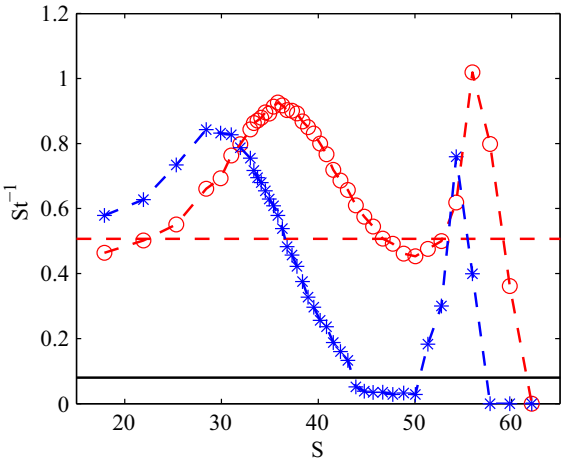

Fig. 11 Frequency response of the aluminum SJ actuator for the single-orifice configuration. Red "circle" markers represent the $H/d = 0.75$ case, "asterisk" stand for $H/d = 2.25$. The dashed line and the continuous line represent the incompressible solution and the formation criterion limit, respectively. (Color figure online)

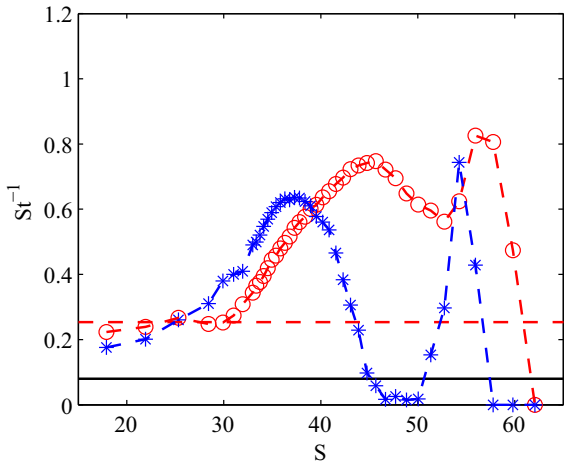

Fig. 12 Frequency response of the aluminum SJ actuator for the double-orifice configuration. The "circle" markers represent the $H/d = 0.75$ case, "asterisk" stand for $H/d = 2.25$. The dashed line and the continuous line represent the incompressible solution and the formation criterion limit, respectively

can be easily extended to the brass diaphragm case: at low frequencies, the jet tends towards the incompressible solution whatever the cavity height is, while, for frequencies between the resonance peaks, the Holman criterion is satisfied for $H/d \leq 2.25$. In general, the brass device satisfies the formation criterion for more conditions with respect to the aluminum one. Note that in the Stokes–Strouhal plane there are some data points slightly below the Holman criterion line, corresponding to a well established jet. These situations occur because the constant C of the Holman relation depends on geometrical factors and on the operation frequency, and thus it could be less than 0.08.

7 Resonance frequencies prediction

Equations (16) and (17) can be used to predict the device resonance frequencies, once the device characteristics are known. A comparison between the analytical values and the experimental ones for the three frequencies is shown in Tables 5 and 6, for the brass and the aluminum actuators respectively, varying the dimensionless cavity height. The effective orifice lengths needed to calculate the Helmholtz frequencies, Eqs. (14) and (15), have been evaluated by using the relationship:

Table 5 Comparison between the analytical and experimental frequency values for the brass device and various cavity heights, f (Hz). The 1st line refers to the analytical data, the 2nd to the experimental ones

Case	Brass			
	f_1	f_2	f_H	$\lvert f_2^2 - f_H^2 \rvert$
H/d = 0.75	1339	1898	1433	1.55e6
	–	1953	1420	1.80e6
H/d = 1.50	1036	1815	1048	2.20e6
	–	1838	1078	2.22e6
H/d = 2.25	883	1806	887	2.47e6
	–	1838	946	2.48e6
H/d = 3.00	796	1804	798	2.62e6
	–	1736	822	2.34e6
H/d = 3.75	744	1803	745	2.70e6
	–	1736	744	2.46e6

Table 6 Comparison between the analytical and experimental frequency values for the aluminum device and various cavity heights, f (Hz). The 1st line refers to the analytical data, the 2nd to the experimental ones

Case	Aluminum			
	f_1	f_2	f_H	$\lvert f_2^2 - f_H^2 \rvert$
H/d = 0.75	1190	2139	1424	2.55e6
	–	2083	1420	2.32e6
H/d = 1.50	999	1864	1041	2.39e6
	–	1953	1078	2.65e6
H/d = 2.25	866	1819	881	2.53e6
	–	1838	946	2.48e6
H/d = 3.00	786	1805	793	2.63e6
	–	1838	822	2.70e6
H/d = 3.75	736	1799	740	2.69e6
	–	1838	744	2.82e6

$$l_e/d = h/d + \Delta l_e \tag{20}$$

where $l_e = l_{e,1} = l_{e,2}$, and Δl_e has been set equal to 0.62 for the highest H / d, and, assuming a linear variation, equal to 1.2 for the lowest H / d.

Overall, the comparison between measured and analytically predicted resonance frequencies is quite satisfactory, especially at the highest values of H / d. More importantly, note that the first frequency f_1 is

strictly close to the Helmholtz frequency, namely $f_3 = f_H$, except in the case of aluminum device at the shortest cavity height. The distance between these two frequencies decreases with increasing H / d because it depends on the coupling degree between the acoustic and the structural oscillators, and of course such a coupling diminishes with increasing H / d. As a significant consequence, the experimental data of frequency response exhibit two resonance peaks only (in fact, the column of f_1 is void in Tables 5 and 6, one at the Helmholtz frequency (scaled as usual by the factor $\sqrt{2}$), and the other at the modified (coupled) structural frequency.

Looking at Eq. 16, it is interesting to study the evolution of the eigenvalues distance as a function of the cavity height, as done by de Luca et al. [21] and Crowther and Gomes [28]. In particular, the distance between the first two eigenvalues $|\omega_1^2 - \omega_2^2|$, for the $\omega_w \ll \omega_H$ case, depends on the cavity height H / d and scales as $\simeq 1/(H/d)$; on the contrary, when $\omega_w \gg \omega_H$, the eigenvalues distance can be considered constant for high H / d ratios. The studied configurations fall within this last case, but it must be remembered that Tables 5 and 6 report the experimental frequencies corresponding to the eigenvalues ω_2 and $\omega_3 = \omega_H$ and not to the first two. For this reason, although the eigenvalues distance tends towards constant values with increasing H, the evolution is slightly different from that of a single-orifice device. The last column of Tables 5 and 6 contains the distance between the eigenvalues corresponding to the detected resonance frequencies; it is possible to observe how this distance tends to a constant value, for both configurations, as the cavity height increases, mainly related to a reduction of the coupling effects.

Note finally that, due to the relatively high values of Stokes numbers attained in the present tests, the viscosity does not impose any limitation to the jet formation, contrary to the finding of Zhou et al. [17], who identified a formation boundary for Stokes number below 4. However, Zhou et al. [17] considered the presence of distributed head losses in relatively long exit pipes, whereas in the present application head losses are of minor type being limited to exit/entrance effects.

8 Conclusions

A theoretical and experimental characterization of the frequency response of a double-orifice SJ actuator has been presented. Numerical simulations, conducted with OpenFOAM, carried out only for the aim of obtaining overall qualitative insights on the development of the flow field, have allowed the study of the device behavior for short and high cavity heights. It is found that, for standard operation conditions and with a symmetric configuration, the device cavity can be considered as divided in two sub-volumes, each of them operating with its own pressure and orifice velocity. Nevertheless, the two cavities are coupled because the oscillating diaphragm shares the stiffnesses of air in the cavities.

Based on these considerations, an analytical approach has allowed to obtain simple expressions for three resonance frequencies and to provide further insights on the jets formation. The model has been validated through experimental tests carried out on two actuators, having different geometrical and mechanical characteristics. The experimental measurements have been limited by the experimental equipment.

The double-orifice actuators experimentally exhibited two resonance peaks, corresponding to the Helmholtz natural frequency (which is equal to the nominal value multiplied by a factor $\sqrt{2}$ due to the halved volume) and to the modified structural frequency. The third resonance frequency, predicted by the analytical model, was never observed, because it practically coincides in all the tested cases with the uncoupled Helmholtz frequency. In certain frequency ranges, the device response is practically null, due to high fluidic damping effects (for $f_H < f < f_2$). As an important consequence, the jet formation criterion is not satisfied in those ranges, as clearly shown in the Stokes–Strouhal plane.

The jet formation is not limited by viscosity effects because only exit/entrance concentrated minor head losses have been considered.

Acknowledgements The authors wish to thank Prof. Carlomagno for his advise on the design and manufacturing of the dedicated Pitot probes, and Prof. Claudio Leone and Dr. Silvio Genna, of the CIRTIBS research center at the University of Naples "Federico II", for their continuous assistance in solving various technological issues.

Compliance with ethical standards

Conflict of interest The authors declare that they have no conflict of interest.

References

1. Sahni O, Wood J, Jansen KE, Amitay M (2011) Three-dimensional interactions between a finite-span synthetic jet, a crossflow. J Fluid Mech 671:254–287. https://doi.org/10.1017/S0022112010005604
2. Chiatto M, Marchitto L, Valentino G, de Luca L (2011) Influence of piezo-driven synthetic jet on water spray behavior. At Spray 27(8):691–706. https://doi.org/10.1615/AtomizSpr.2017020419
3. Tamburello DA, Amitay M (2008) Active manipulation of a particle-laden jet. Int J Multiph Flow 34(9):829–851. https://doi.org/10.1016/j.ijmultiphaseflow.2008.02.006
4. Chaudhari M, Puranik B, Agrawal A (2010) Heat transfer characteristics of synthetic jet impingement cooling. Int J Heat Mass Transf 53(5–6):1057–1069. https://doi.org/10.1016/j.ijheatmasstransfer.2009.11.005
5. Smith BL, Glezer A (1998) The formation, evolution of synthetic jets. Phys Fluid 10(9):2281–2297. https://doi.org/10.1063/1.869828
6. Cater JE, Soria J (2002) The evolution of round zero-net-mass-flux jets. J Fluid Mech 472:167–200. https://doi.org/10.1017/S0022112002002264
7. Watson M, Jaworski AJ, Wood NJ (2003) A study of synthetic jets from rectangular, dual-circular orifices. Aeronaut J 107:427–434. https://doi.org/10.1017/S000192400001335X
8. Riazi H, Ahmed NA (2011) Numerical investigation on two-orifice synthetic jet actuators of varying orifice spacing, diameter. In: 29th AIAA applied aerodynamics conference. https://doi.org/10.2514/6.2011-3171
9. Sakakibara H, Watanabe T, Nagata K (2018) Supersonic piston synthetic jets with single/multiple orifice. Exp Fluid 59(5):76. https://doi.org/10.1007/s00348-018-2529-9
10. Chaudhari M, Puranik B, Agrawal A (2011) Multiple orifice synthetic jet for improvement in impingement heat transfer. Int J Heat Mass Transf 54(9–10):2056–2065. https://doi.org/10.1016/j.ijheatmasstransfer.2010.12.023
11. Mangate LD, Chaudhari MB (2016) Experimental study on heat transfer characteristics of a heat sink with multiple-orifice synthetic jet. Int J Heat Mass Transf 103:1181–1190. https://doi.org/10.1016/j.ijheatmasstransfer.2016.08.058
12. Girfoglio M, Greco CS, Chiatto M, de Luca L (2015) Modelling of efficiency of synthetic jet actuators. Sens Actuators A Phys 233:512–521. https://doi.org/10.1016/j.sna.2015.07.030
13. Chiatto M, Capuano F, Coppola G, de Luca L (2017) LEM characterization of synthetic jet actuators driven by piezoelectric element: a review. Sensors 17(6):1–31. https://doi.org/10.3390/s17061216
14. Glezer A, Amitay M (2002) Synthetic jets. Annu Rev Fluid Mech 34:503–529. https://doi.org/10.1146/annurev.fluid.34.090501.094913
15. Mohseni K, Mittal R (2015) Synthetic jets: fundamentals, applications. CRC Press, Abingdon
16. Smith BL, Glezer A (2002) Jet vectoring using synthetic jets. J Fluid Mech 458:1–34. https://doi.org/10.1017/S0022112001007406
17. Zhou J, Tang H, Zhong S (2009) Vortex roll-up criterion for synthetic jets. AIAA J 47(5):1252–1262. https://doi.org/10.2514/1.40602
18. Krishnan G, Mohseni K (2009) Axisymmetric synthetic jets: an experimental, theoretical examination. AIAA J 47(10):2273–2283. https://doi.org/10.2514/1.42967
19. Hunt JCR, Wray AA, Moin P (1988) Eddies, streams, convergence zones in turbulent flows. In: Proceedings of the CTR Summer Program, Stanford, CA
20. Sharma RN (2007) Fluid-dynamic-based analytical model for synthetic jet actuation. AIAA J 45(8):1841–1847. https://doi.org/10.2514/1.25427
21. de Luca L, Girfoglio M, Chiatto M, Coppola G (2016) Scaling properties of resonant cavities driven by piezoelectric actuators. Sens Actuators A Phys 247:465–474. https://doi.org/10.1016/j.sna.2016.06.016
22. Ingard U (1953) On the theory, design of acoustic resonators. J Acoust Soc Am 25(6):1037–1061. https://doi.org/10.1121/1.1907235
23. Moffat RJ (1988) Describing the uncertainties in experimental results. Exp Therm Fluid Sci 1(1):3–17. https://doi.org/10.1016/0894-1777(88)90043-X
24. Holman R, Uttukar Y, Mittal R, Smith BL, Cattafesta LN III (2005) Formation criterion for synthetic jets. AIAA J 43(10):2110–2116. https://doi.org/10.2514/1.12033
25. Gallas Q, Holman R, Nishida T, Carroll B, Sheplak M, Cattafesta L III (2003) Lumped element modeling of piezoelectric-driven synthetic jet actuators. AIAA J 41(2):240–247. https://doi.org/10.2514/2.1936
26. Persoons T (2012) General reduced-order model to design, operate synthetic jet actuators. AIAA J 50(4):916–927. https://doi.org/10.2514/1.J051381
27. Kooijman G, Ouweltjes O (2009) Finite difference time domain electroacoustic model for synthetic jet actuators including nonlinear flow resistance. J Acoust Soc Am 125(4):1911–1918. https://doi.org/10.1121/1.3081514
28. Crowther WJ, Gomes LT (2008) An evaluation of the mass, power scaling of synthetic jet actuator flow control technology for civil transport aircraft applications. Proc Inst Mech Eng Part I Syst Control Eng 222:357–372. https://doi.org/10.1243/09596518JSCE519